J-INTEGRAL APPROACH TO ESTIMATION OF TENSILE STRAIN CAPACITY IN STRAIN-BASED DESIGN

M. Reza Hirmand[1], William R. Tyson[1], Su Xu[1], Timothy S. Weeks[2]

[1]CanmetMATERIALS, Natural Resources Canada, Hamilton, ON, Canada
[2]National Institute of Standards and Technology, Boulder, CO, USA

ABSTRACT: This paper revisits previous numerical predictions and experimental measurements of tensile strain capacity (TSC) in curved wide plate (CWP) specimens. The work is motivated by the arguably surprising conclusion in (Liu, Wang, Horsley, et al. 2012) that better predictions can be made from toughness data extracted from Charpy V-notch (CVN) tests compared with fracture mechanics tests using single-edge-notched tensile (SE(T)) specimens. The *J*-integral is used to describe driving and resistance forces rather than the CTOD used previously (Liu, Wang, Song, et al. 2012; Liu, Wang, Horsley, et al. 2012). Small-specimen toughness data is used to make numerical predictions of full-scale CWP specimens based on instability and initiation limit state methods. Several important factors that impact the utility of the *J*-integral approach are addressed. These include applicability of *J*-integral in gross plasticity, consistency of the flaw constraint conditions in resistance curve measurements and CWP tests, the type of stress-strain relationships used, shape of the flaw, and mechanical properties at the flaw tip. The *J*-integral approach is shown to yield predictions that agree better with experimental measurements than previous CTOD-based calculations while avoiding the controversy over the definition of CTOD. Strain-based design using *J* is thus validated, supporting first-principles estimation of initiation and instability strains using only small-scale SE(T) data and *J* calculations.

1.   INTRODUCTION

This paper revisits previous numerical predictions and experimental measurements of tensile strain capacity in curved wide plate (CWP) specimens. The tests (Weeks, McColskey, and Richards 2011; Wang et al. 2011) were under a U.S. Department of Transportation (DOT) and Pipeline Research Council International (PRCI) co-sponsored project using specimens taken from American Petroleum Institute (API) 5L X100 pipes (API 2012) with outer diameter 36 in (914 mm) and wall thickness 19.1 mm. A detailed description of the specimens' geometry and test procedure may be found in (Weeks, McColskey, and Richards 2011). Ductile instability and initiation limit state solution methods were presented in (Liu, Wang, Horsley, et al. 2012; Liu, Wang, Song, et al. 2012) to numerically predict the tensile strain capacity (TSC) of CWP specimens. The present study is motivated by the arguably surprising conclusion in (Liu,

Technology for Future and Ageing Pipelines 2021
J-integral Approach to Estimation of Tensile Strain Capacity in Strain-Based Design
M.R. Hirmand, W.R. Tyson, S. Xu and T.S. Weeks

Wang, Horsley, et al. 2012) that better predictions can be made from toughness data extracted from Charpy V-notch (CVN) tests compared with fracture mechanics tests using single-edge-notched tensile (SE(T)) specimens. In this work, the J-integral is employed to describe driving and resistance forces rather than the crack-tip opening displacement (CTOD) used previously (Liu, Wang, Song, et al. 2012; Liu, Wang, Horsley, et al. 2012). Small-specimen toughness data are used to make numerical predictions of full-scale CWP specimens, based on instability and initiation limit state methods. A review of TSC prediction methodologies has been presented in (Park and Gianetto 2019) highlighting the merits of the J-integral approach. By using the SE(T) resistance curves, this study sheds some light on the transferability of resistance curves obtained from small scale specimens to larger scales. In addition, several important factors that impact the utility of the J-integral approach are addressed. These include applicability of J-integral in gross plasticity, consistency of the flaw constraint conditions in resistance curve measurements and CWP tests, the type of stress-strain relationships used, shape of the flaw, and mechanical properties at the flaw tip. The present J-integral approach is shown to yield predictions of TSC based on ductile instability and initiation limit state methods that agree better with experimental measurements than previous CTOD-based calculations. Strain-based design using J is thus validated, supporting first-principles estimation of initiation and instability strains using only small-scale SE(T) data and J calculations for CWP. Additionally, the J-integral approach avoids controversy over the definition of CTOD and the empirical conversions of CVN-to-CTOD data. Other factors favouring J over CTOD include simpler instrumentation and interpretation of small-scale tests (single-gauge versus dual-gauge set-up) and general applicability with no limitation of steel grade.

2.   STRUCTURE OF THE TSC PREDICTION APPROACH

In the ductile instability solution method (Liu, Wang, Horsley, et al. 2012; Wang et al. 2011), the TSC is defined by the tangency point of the crack driving force curve and the fracture toughness (resistance) curve. Different measures can be used to characterize driving "force" and resistance, the most common being CTOD and J-integral. The J-integral driving force ($J_D(e, a)$, where e is the remote strain and a is the length of the crack) is dependent on the geometry, material properties, and loading conditions of the particular application at hand. The J-integral resistance curve ($J_R(\Delta a)$, where Δa is the length of crack growth) is dependent on material and test conditions (temperature, strain rate, and geometry). The *ductile instability* limit state (*i.e.*, the tensile strain capacity (TSC) and corresponding crack growth at unstable failure) is obtained by solving the following system of equations for e and Δa:

$$\begin{cases} J_D(e, a_0 + \Delta a) = J_R(\Delta a) \\ \dfrac{\partial J_D(e, a_0 + \Delta a)}{\partial \Delta a} = \dfrac{d J_R(\Delta a)}{d \Delta a} \end{cases} \tag{1}$$

where a_0 is the initial length of the crack.

The *initiation* limit state is intended to give a conservative estimate of the strain capacity of the plate. It is given by the strain at which the driving force J_D of the initial (stationary) flaw reaches the initiation fracture toughness defined to be the J_R value at a small amount of crack growth Δa_{init} (Liu, Wang, Horsley, et al. 2012; Wang et al. 2011). The following equation is solved for e:

$$J_D(e, a_0) = J_R(\Delta a_{init}). \tag{2}$$

In practice, the specific value of Δa_{init} is chosen based on engineering judgment. Potential candidates often used in the literature are 0.5 mm (Liu, Wang, Horsley, et al. 2012) or 0.2 mm (Liu, Wang, and Long 2010). This choice will be further discussed later in Section 4.

Technology for Future and Ageing Pipelines 2021
J-integral Approach to Estimation of Tensile Strain Capacity in Strain-Based Design
M.R. Hirmand, W.R. Tyson, S. Xu and T.S. Weeks

The constraint conditions of the flaw in the small-scale specimen used to obtain J_R should be the same as those in the large-scale application (the CWP in this case). Shen et al. (Shen et al. 2008) concluded that the constraint in a SE(T) specimen with ratio of span between load points to width (H/W) equal to 10 provides a reasonable match to that for a circumferential crack in a pipe of the same thickness subject to tensile loading. Resistance J_R curves previously reported in (D. Y. Park et al. 2011) for X100 pipe girth welds using SE(T) specimens with W=17.2 mm and H/W=10 have been used in the present study. They include results with flaws in base metal (BM), heat affected zone (HAZ) and weld metal (WM) of the pipe girth welds. A power law equation of the form $J_R = c_1(\Delta a)^{c_2}$ was used for curve fitting the experimentally measured J_R curves. For more details regarding the material, specimen preparation and testing performed, the reader is referred to (D. Y. Park et al. 2011). The initial flaw depths in SE(T) and CWP specimens are not necessarily equal to the targeted values (in some cases, they show more than 100% difference). In addition, the width of SE(T) and CWP specimens are not equal. Thus, the following procedure was applied to enhance consistency of flaw-tip constraint conditions in SE(T) and CWP specimens. The J_R curve-fitting coefficients c_1 and c_2 were first made functions of the initial flaw depth by applying a linear best fit to measured SE(T) data. For each CWP test, an equivalent SE(T) flaw-depth was then obtained by requiring that $a_0^{\text{SE(T)}}/W = a_0^{\text{CWP}}/t$. Given a_0^{CWP}, the coefficients c_1 and c_2 required to construct the J_R curve were obtained using an equivalent SE(T) flaw-depth of $a_0^{\text{SE(T)}} = a_0^{\text{CWP}}W/t \approx 0.9\, a_0^{\text{CWP}}$.

3. DEVELOPMENT OF CWP DRIVING FORCE CURVES

3.1 Material model and properties

The material model used was the same as in the development of SE(T) J_R curves by CANMET (Shen, Gianetto, and Tyson 2008):

$$\varepsilon = \begin{cases} \dfrac{\sigma}{E} & \sigma < \sigma_y \\ \dfrac{\sigma_y}{E}\left(\dfrac{\sigma}{\sigma_y}\right)^n & \sigma \geq \sigma_y, \end{cases} \qquad [3]$$

where ε and σ are the true strain and true stress, respectively, E is the Young's modulus, σ_y is the yield strength, and n is the strain-hardening exponent. In all cases, elastic properties were $E = 206.7$ GPa and $\nu = 0.3$. Table 1 summarizes the CANMET model tensile properties considered for the pipe BM (X100), HAZ, and WM at room temperature. It should be noted that, in addition to pipe-to-pipe strength variation, there is a considerable range of yield stress values associated with circumferential location even on a single pipe (Gianetto et al. 2011). Hence, the properties given in Table 1 should only be regarded as representative properties of the X100 steel. The constitutive equation proposed in (Xu and Tyson 2015; Xu, Bouchard, and Tyson 2004) was used to adjust the material properties at different temperatures by adding the thermal component of the flow stress $\Delta\sigma_{\text{th}}$ to the yield strength at room temperature. At $T = -20$ °C, the thermal stress is only about 7 MPa.

Table 1. Tensile properties (longitudinal) of different regions of X100 pipe in CWPs

		Tensile Properties	
		σ_y (MPa)	n
Base Metal & HAZ		781	17.32
Weld metal	Round 1	835	16.10
	Round 2	827	19.61

3.2   Calculation of J-integrals in CWP specimens

To obtain path independent J-integrals in incremental plasticity, it is advised to ensure that the contour-integral used is large enough to surround the plastic zone (*i.e.*, pass through the elastic region only) so that a "saturated value" of J is reached (Brocks and Scheider 2001). In the CWP specimens used in this work, this is not possible since gross plasticity is encountered for the loading levels of interest. In that case, path dependence increases strongly and a saturated value of J cannot be reached. An example of this situation is shown in Figure 1 using one of the FE models considered in the present study.

To circumvent the issue of strong path dependence of J at high plastic strains the following approach is employed. The plastic component of J is evaluated as a function of area under the load versus plastic CMOD curve and added to the well-established elastic component (see Equation 4 below) based on the method in ASTM E1820 (ASTM 2015). Parameters are obtained using the procedure described in (Zhang et al. 2012) for small scale, contained plasticity in which J-integral values obtained from direct contour integral calculations are valid. At larger strains where gross plasticity is encountered, J values are calculated from the developed relationship rather than direct contour integral calculations. This method of calculating J_D integrals is similar to that used in calculating J_R curves and ensures that the same definitions of J, whatever they mean, are being calculated in constructing J_D and J_R curves throughout the course of loading. Given that the constraint conditions in SE(T) and CWP specimens (*i.e.*, a/W and a/t, respectively) have been designed to be similar (see also Section 2), the calculated J values provide a parameter that describes the same crack-tip conditions in the small-scale test and the CWP application.
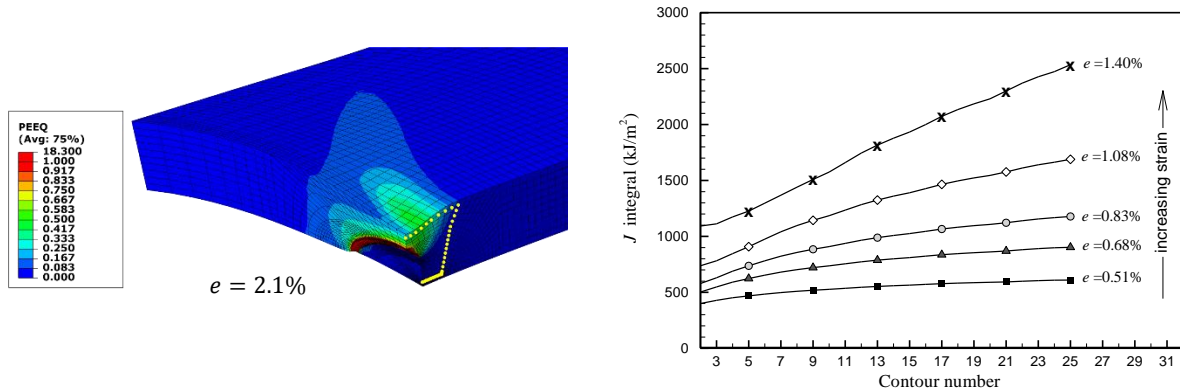

Figure 1. An example of loss of path dependence of J owing to reaching gross plasticity. Only a quarter of the plate is shown. The yellow circles in the top figure mark the boundary of the largest contour integral domain (contour number 25). Note that the contour integral cannot touch the free surface, otherwise J calculations are not valid (Brocks and Scheider 2001). Flaw size: a/t=8/19.1 (*i.e.*, 0.42), $2c/t$=50/19.1 (*i.e.*, 2.62). BM properties were used (see Table 1)

The formula for determining J from load versus plastic CMOD data for a stationary crack in a CWP is (ASTM 2015)

$$J = J_e + J_{pl} = \frac{K^2(1-v^2)}{E} + \frac{\eta A_{pl}}{W'(t-a)},$$
[4]

in which K is the stress intensity factor in the elastic regime which may be found in (Wang et al. 2011) for semielliptical flaws, W' and t are the specimen arc-width and thickness, respectively, a is the flaw depth and A_{pl} is the area under the load versus plastic CMOD curve as described in (ASTM 2015). With $J_{pl} = J - J_e$ obtained from

FEA, η may be taken to be the slope of the best linear fit to J_{pl} versus $A_{pl}/W'(t-a)$ data points obtained at various load levels. Because the flaws in the CWP specimens are extended in fatigue to sharpen the tip (Weeks, McColskey, and Richards 2011), the geometry of the flaws produced in practice vary in shape somewhat as opposed to being strictly semielliptical or canoe-shape. Semielliptical flaw geometries have been employed in most works in the literature (see *e.g.*, (Liu, Wang, Song, et al. 2012; Nourpanah and Taheri 2010)) and are assumed to represent the actual flaw geometry in the remainder of this study.

The matrix of FE simulations considered for this purpose is defined by $a \in \{2,3,4,5,6,7,8,9\}$ mm, $2c \in \{30,50,75\}$ mm and $\sigma_y \in \sigma_y(\{HAZ, WM, BM\} \times \{weld\ round\ 1\ \&\ 2\})$. A typical finite element (FE) model of a CWP specimen along with a schematic of the flaw shape is shown in Figure 2. Only a quarter of the plate is considered exploiting symmetry of the boundary conditions. The total displacement applied in each case was large enough to induce sufficient plastic deformation at the crack tip without undermining the "nearly-contained plasticity" conditions in view of the discussion in Section 2.2. It was confirmed that the "saturated" value of J was reached by verifying that the values obtained from the three largest contour integrals differed by no more than 5 % (see Figure 1). Having η for all combinations of a/t and $2c/t$, a curve fitting approach similar to the one in (Zhang et al. 2012) was conducted leading to

$$\eta\left(\frac{a}{t}, \frac{2c}{t}\right) = 0.2246 + 0.3338\left(\frac{a}{t}\right) - 1.7198\left(\frac{a}{t}\right)^2 + 0.2270\sqrt{ln\left(1 + 8.0622\frac{2c}{t}\right)}. \tag{5}$$

(a)   (b)
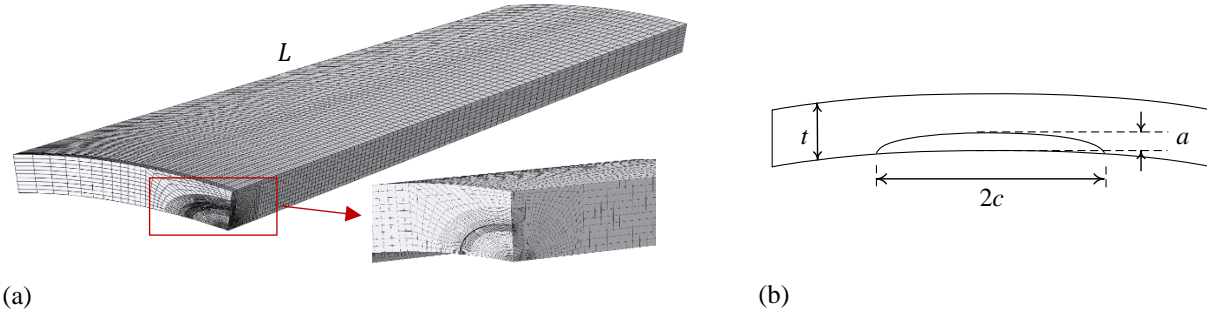
Figure 2. a) Typical Finite Element model of a CWP (only a quarter of the plate is modelled to take advantage of symmetry), and b) schematic of semielliptical flaw

3.3 Obtaining J_D curves for CWP specimens

J-integrals used in the construction of J_D curves were calculated from Equations 4-5 (and not the contour integral calculations) in which the plastic load versus CMOD data were obtained from FEA. The J_D curves are derived by interpolating J values obtained for stationary cracks of different sizes. Applying standard dimensional analysis, and given that R/t is constant in the present application, the general form of the J_D curve is written as

$$J' \equiv \frac{J}{\sigma_y t} = f\left(\frac{a}{t}, \frac{2c}{t}, n, e\right). \tag{6}$$

Note that J in general varies quadratically with the applied strain (which is taken to be equal to the remote strain e) when the pipe deformation is elastic with confined plasticity at the flaw tip, and linearly when plasticity develops through the net section prior the occurrence of ligament instability. The latter is relevant to strain based design (Nourpanah and Taheri 2010). With that consideration in mind, the general form of f is taken to be (Nourpanah and Taheri 2010)

Technology for Future and Ageing Pipelines 2021
J-integral Approach to Estimation of Tensile Strain Capacity in Strain-Based Design
M.R. Hirmand, W.R. Tyson, S. Xu and T.S. Weeks

$$f = \beta_0 + \beta_1 e, \tag{7}$$

where β_0 and β_1 are functions of a/t and n given by

$$\beta_0 = \theta_1 + \theta_2 \frac{a}{t},$$
$$\beta_1 = (\theta_3 + \theta_4 n) + (\theta_5 + \theta_6 n)\left(\frac{a}{t}\right) + (\theta_7 + \theta_8 n)\left(\frac{a}{t}\right)^2. \tag{8}$$

In the above, $\theta_1, \dots, \theta_8$ are functions of $2c/t$ given by

$$\theta_i = \alpha_{3i-2} + \alpha_{3i-1}\left(\frac{2c}{t}\right) + \alpha_{3i}\left(\frac{2c}{t}\right)^2, \tag{9}$$

where $\alpha_{3i-2}, \alpha_{3i-1}, \alpha_{3i}$, i =1:8, are interpolation coefficients. The matrix of FE simulations considered to calibrate these coefficients was the same as that used in determining η (see Section 2.3). In each case, the applied strain was increased high enough to induce significant plastic strain in the ligament. Only the post-elastic data points (*i.e.*, points where J varies linearly with applied strain) were considered in calibrating the coefficients. The results are summarized in Table 2. Caution should be taken when using approximate Equations 6-9 for calculations outside the ranges considered in the FE matrix.

Table 2. Curve fitting coefficients for approximate J_D curves

	α_{3i-2}	α_{3i-1}	α_{3i}
θ_1	-0.0001	0.0093	-0.0099
θ_2	-0.0005	-0.056	0.0504
θ_3	0.0046	-0.0275	0.0287
θ_4	-0.0001	0.001	-0.0011
θ_5	-0.0713	0.4193	-0.3749
θ_6	0.0021	-0.0192	0.0221
θ_7	0.2204	-1.2751	1.3577
θ_8	-0.0068	0.0781	0.0887

4.   CWP MEASUREMENTS

Table 3 includes the details of the geometries and the remote strains measured below and above the flaw in 29 CWP experiments performed by NIST in the DOT/PRCI sponsored project (Weeks, McColskey, and Richards 2011; Wang et al. 2011). Figure 3 shows the data of CWP-09 (after some post-processing to "shift" the curves so that they pass through the origin) as a representative case. The last two columns of the Table show the numerical predictions obtained based on the ductile instability and initiation limit state methods. Further discussion on the numerical predictions will be presented in Section 5.

The maximum remote strains measured below and above the flaw are different in almost all tests. On average, there is a discrepancy of ~50 % between measurements above and below the flaw. This non-symmetric behaviour has been attributed to differences in the yield strengths and work hardening behaviours above and below the flaw (Liu, Wang, Horsley, et al. 2012). Due to flatness (large n values) of the stress-strain curves, the strains would be significantly different at same stress.

Technology for Future and Ageing Pipelines 2021
J-integral Approach to Estimation of Tensile Strain Capacity in Strain-Based Design
M.R. Hirmand, W.R. Tyson, S. Xu and T.S. Weeks

Table 3. Summary of CWP specifications and measured strains (in percent). All dimensions in mm.

| Specimen ID	target $a \times 2c$	Temperature (°C)	Flaw location	Weld Round	Measured a_0	Measured thickness	Remote strain-BW*	Remote strain-AW**	Predicted TSC range (ductile instability)		Predicted TSC range (initiation) $\Delta a_{init} = 0.2$	
CWP-0	3×50	-20	BM	-	3.11	19.00	3.9	4.34	[3.23	4.40]	[1.49	1.59]
CWP-00	3×50	25	BM	-	3.00	19.13	3.65	4.79	[3.01	4.04]	[1.44	1.53]
CWP-1	6×30	25	WM	1	6.36	18.97	1.32	2.34	[1.09	1.30]	[0.81	0.81]
CWP-2	3×50	-20	HAZ-BW	1	2.98	18.97	3.07	3.81	[2.87	3.71]	[1.67	1.73]
CWP-5	3×50	-20	HAZ-BW	1	2.91	19.00	2.89	1.74	[2.98	3.85]	[1.75	1.81]
CWP-6	2×75	25	WM	1	2.12	19.03	2.66	1.92	[2.54	2.86]	[2.13	2.08]
CWP-7	2×75	-20	WM	1	2.23	19.10	2.31	4.23	[2.26	2.59]	[1.33	1.39]
CWP-8	2×75	25	HAZ-BW	1	2.17	18.93	2.78	5.56	[3.98	4.74]	[3.10	3.19]
CWP-9	2×75	-20	HAZ-AW	1	1.97	19.01	4.81	2.09	[4.35	5.20]	[3.06	3.23]
CWP-10	6×30	-20	HAZ-AW	1	6.06	18.98	1.77	1.76	[1.90	2.77]	[0.76	0.78]
CWP-11	3×50	-20	WM	1	3.14	18.96	2.44	2.62	[1.96	2.33]	[1.27	1.30]
CWP-12	6×30	-20	HAZ-BW	1	6.14	18.90	3.22	3.71	[1.85	2.69]	[0.75	0.76]
CWP-13	3×50	-40	WM	1	2.95	18.77	2.05	2.47	[1.45	1.61]	[1.40	1.33]
CWP-14	3×50	-40	WM	1	3.21	18.99	2.55	2.35	[1.60	1.84]	[1.23	1.22]
CWP-16	3×50	25	WM	1	3.39	18.97	2.31	2.23	[1.88	2.17]	[1.45	1.45]
CWP-17	3×50	-40	HAZ-AW	1	3.09	18.98	2.70	2.89	[2.83	3.72]	[1.51	1.58]
CWP-18	3×50	-40	WM	1	2.81	18.84	3.97	3.15	[1.39	1.54]	[1.48	1.37]
CWP-19	3×50	-20	WM	1	3.27	18.96	2.33	2.26	[1.89	2.26]	[1.24	1.26]
CWP-20	3×50	25	WM	2	2.88	18.92	1.86	1.45	[1.97	2.27]	[1.54	1.55]
CWP-21	3×50	25	HAZ-AW	2	3.09	18.81	1.80	1.89	[2.54	3.44]	[1.17	1.25]
CWP-22	3×50	-20	WM	2	2.96	18.98	1.92	1.79	[1.75	2.12]	[1.00	1.05]
CWP-23	3×50	-20	HAZ-AW	2	2.94	18.93	2.18	2.26	[2.65	3.53]	[1.32	1.39]
CWP-24	6×30	25	WM	2	6.36	19.23	1.50	1.63	[1.80	2.40]	[0.91	0.93]
CWP-25	6×30	25	HAZ-BW	2	6.29	19.20	1.84	1.28	[1.56	2.11]	[0.84	0.83]
CWP-26	6×30	-20	WM	2	6.15	19.22	1.41	1.85	[1.83	2.41]	[0.94	0.96]
CWP-27	6×30	-20	HAZ-AW	2	6.19	19.23	2.14	2.14	[2.17	3.43]	[0.65	0.68]
CWP-28	3×50	-40	WM	2	3.08	19.17	2.21	1.93	[1.46	1.62]	[1.30	1.27]
CWP-29	3×50	-40	HAZ-AW	2	3.35	19.14	2.53	2.58	[2.59	3.36]	[1.50	1.54]

* BW: Below the Weld
**AW: Above the Weld
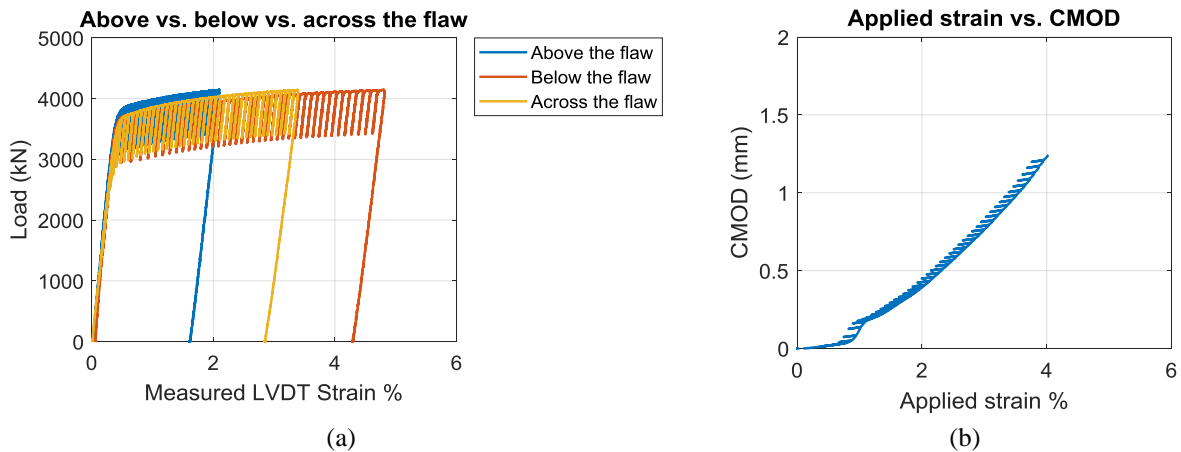
Figure 3. Post-processed data of CWP-09

The difference in the LVDT measurements above and below the weld raises the question, what should be taken as the TSC of the plate? In this work, the WM always overmatches the BM and so at a constant stress the strain is lower in

the WM. In the case of a HAZ flaw, the WM "shields" the flaw from strains in the plate on the opposite side of the weld from the flaw. It may be assumed that the flaw behaves as if it were located in a homogeneous plate with properties the same as those of the plate next to the flaw. In that case, the TSC of the plate is taken to be the strain measured in the half-plate on the flaw side of the weld. In the case of a WM flaw, it is assumed that the flaw-tip deformations are controlled by the WM tensile properties. For constant stresses, the strain in the BM half-plates on the two sides of the weld are different depending on whether the half-plate is weaker or stronger than average plate properties. The average of the strains measured above and below the flaw should give a value close to that expected for a plate of average tensile properties and is taken to be the TSC of the plate. To account for the difference in the tensile properties of the remote regions, the TSC obtained based on WM properties is transformed to the equivalent BM strain using Equation 3 (Hirmand, Tyson, Xu, et al. 2021).

5.   RESULTS AND DISCUSSION

The ductile instability and initiation limit state methods presented in Section 2 were applied to each CWP test. For the ductile instability solution, the system of equations defined by Equation 1 was solved numerically using a Newton-Raphson scheme. In each case, the TSCs were estimate by assuming a ± 10 % variation in the coefficients c_1 and c_2 of the J_R curves to account for experimental uncertainties in J_R values due to interpolation for flaw depths, variations of the properties etc. The predicted TSCs obtained are compared with the measured remote strains in Figure 4(a). The vertical error bars show the remote strains measured below and above the flaw. The horizontal error bars show the uncertainty in predicted TSC arising from the assumed ± 10 % uncertainty in the J_R curve coefficients. The data corresponding to Figure 4(a) are included in Table 3. An interesting observation is that the slight uncertainties introduced can lead to relatively large differences (~25 % on average, and up to 60 % in some cases *e.g.*, CWP-27) in predicted TSC values. Furthermore, Figure 4(b) shows the predicted ductile instability limit strains (without considering the variations in c_1 and c_2) versus the measured TSCs. Note that, as discussed above, for the HAZ tests the measured TSC is the remote strain measured in the half-plate next to the flaw. For WM tests the TSC is the average of remote strain on both sides of the weld.
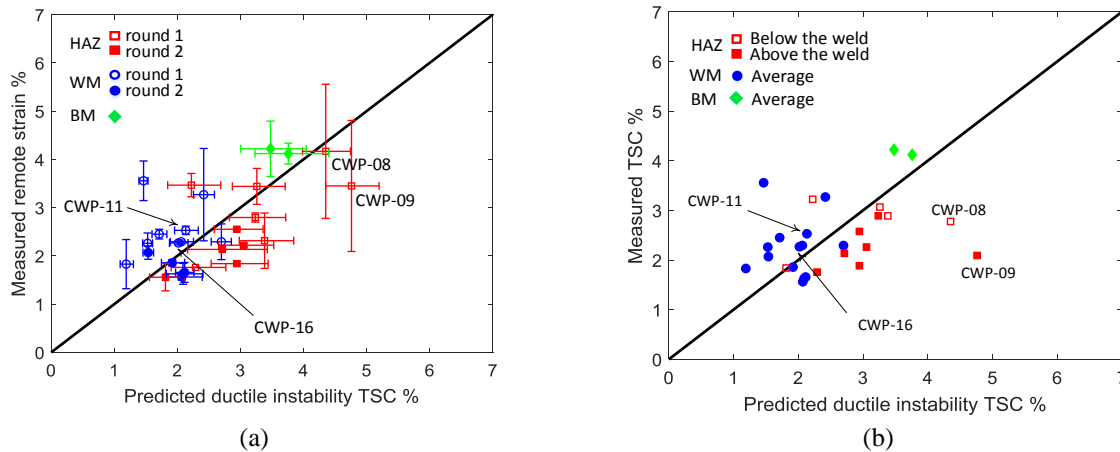

Figure 4. a) Measured remote strains versus predicted TSCs and, b) measured TSCs versus predicted TSCs of CWP specimens

The significance of the four tests CWP-08, CWP-09, CWP-11, and CWP-16 marked in Figure 4(a)-(b) is as follows. The tests CWP-08 and CWP-09 both have HAZ flaws and show the largest discrepancy between the strains measured above and below the flaw, see Figure 4(a). In addition, the measured termination strains are much below the predicted instability strains in these tests, see Figure 4(b). On the other hand, in CWP-11 and CWP-16, which both have WM flaws, the two measured strains are nearly equal. The CMOD versus applied strain (*i.e.*, end displacement divided by

the plate's length) and load versus applied strain of these two groups of tests are shown in Figure 5 and Figure 6. As explained in (Weeks, McColskey, and Richards 2011), these curves were monitored during the tests to control test termination: at the TSC, the load curve should become flat whereas the CMOD curves should reach a vertical asymptote. These two groups appear to identify two extreme conditions in CWP specimens. In the first group, namely, CWP-08 and CWP-09, the half-plates have significantly different tensile properties leading to different strains above and below the flaw. This seems to have in turn led to premature termination of the test given that the CMOD curves have not reached their vertical asymptotes at termination in spite of the fact that load versus applied strain curve has become nearly flat. This aligns well with the observation that the predicted TSCs are relatively larger than the measured TSCs for these two test as can be seen in Figure 4(b). In contrast, the CMOD curves corresponding to the second group of tests (CWP-11 and CWP-16; these tests had in fact an unexpected failure (Weeks, McColskey, and Richards 2011)) have reached an asymptotic region at termination. The predicted and measured TSCs are in excellent agreement in these two tests. This is also the case for the BM-only tests where the plate inhomogeneity is presumably minimized.
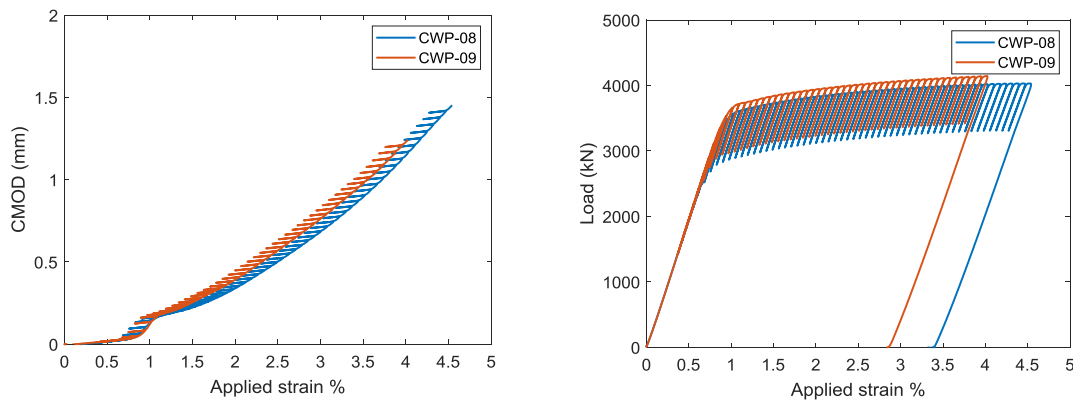

Figure 5. a) CMOD versus applied strain and b) load versus applied strain for CWP-08 and CWP-09
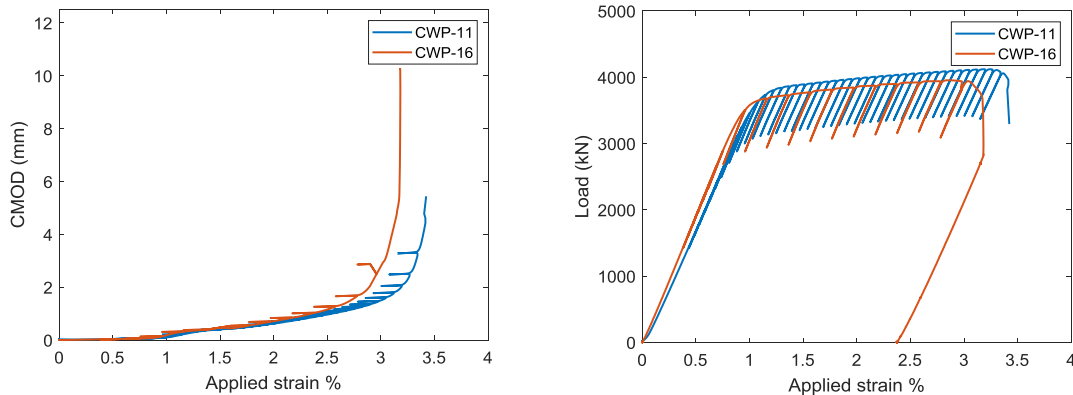

Figure 6. a) CMOD versus applied strain and b) load versus applied strain for CWP-11 and CWP-16

The scatter in Figure 4(a)-(b) may be attributed to the inevitable and non-quantified scatter in various test conditions (*e.g.*, tensile properties of the X100 steel, flaw shape etc.). A similar type of behaviour has been reported in [1, Figure 19 and 20] for CTOD-based ductile instability limit state solutions using values of CTOD obtained from J_R curves measured in SE(T) tests. To determine which of the two approaches (J-based or CTOD-based) gives a better representation of experimental TSCs, we calculate a "normalized error" n_E between the measured and predicted TSC data points in Figure 4(b) and in Table 9 of (Liu, Wang, Horsley, et al. 2012) as $n_E = \sqrt{\sum(\text{TSC}_{\text{num}} - \text{TSC}_{\text{meas}})^2} / \sqrt{\sum(\text{TSC}_{\text{meas}})^2}$. This definition of error gives a measure of the agreement between the numerical predictions and

Technology for Future and Ageing Pipelines 2021
J-integral Approach to Estimation of Tensile Strain Capacity in Strain-Based Design
M.R. Hirmand, W.R. Tyson, S. Xu and T.S. Weeks

experimental measurements; the better the agreement, the smaller the error. Excluding CWP-08 and CWP-09 which were identified as outliers, the normalized error is 0.23 for the present J-based approach and 0.36 for the CTOD-based approach. Hence, it is concluded that ductile instability TSC deduced from J is more predictive than that deduced from CTOD.

Next, the TSCs obtained using the initiation limit state method are presented. The choice of the initiation crack growth Δa_{init} has a significant impact. Results using Δa_{init}=0.2 mm and Δa_{init}=0.5 mm are shown in Figure 7. For completeness, the average and range of measured remote strains are used in these figures (as in Figure 4(a)). Note that the measured strains are at failure while the predicted initiation strains are at initiation, hence the former should be larger than the latter. As opposed to Δa_{init}=0.5 mm (which has been suggested in (Liu, Wang, Horsley, et al. 2012; Wang et al. 2011)), Δa_{init}=0.2 mm yields initiation strain predictions that are conservatively lower than the measured remote strains. Thus, Δa_{init}=0.5 mm appears to be too large to conservatively predict the instability strain in the present application. The predicted initiation strains are nearly insensitive to uncertainties in the resistance curves so that the horizontal error bars in Figure 7 are negligible. This is because a small change in the critical J does not entail a significant change in the corresponding strain on the J_D curve of the initial flaw.
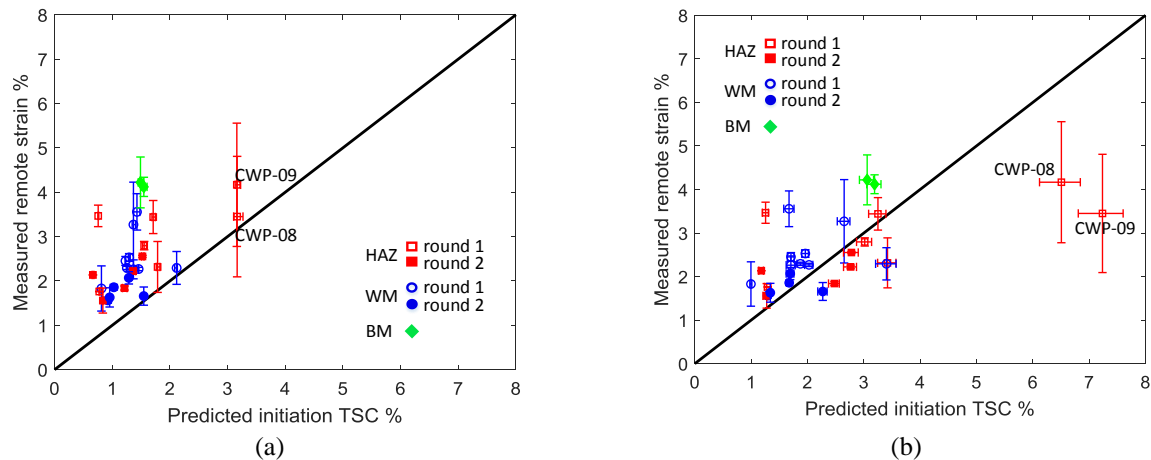

Figure 7. Comparison of predicted initiation strains with measured strains using a) Δa_{init}=0.2 and b) Δa_{init}=0.5

5.   CONCLUSIONS

The present re-analysis of available CWP data demonstrates that J can be usefully calculated beyond "validity" limits and allows CWP tensile strain limits to be estimated with reasonable accuracy. Thus, strain based design using J is validated, supporting first-principles estimation of initiation and instability using only small-scale SE(T) data and J calculations for CWP. Application of the present methodology to pipelines requires further analysis for pipe geometries to obtain robust driving-force estimates and investigate the practical methodology to predict instability strains.

6.   ACKNOWLEDGEMENTS

Technology for Future and Ageing Pipelines 2021
J-integral Approach to Estimation of Tensile Strain Capacity in Strain-Based Design
M.R. Hirmand, W.R. Tyson, S. Xu and T.S. Weeks

7. REFERENCES

Anon, API Specification 5L, "Specification for Line Pipe", Washington, DC. *American Petroleum Institute* (API), 2012."

Anon, "ASTM E1820: Standard Test Method for Measurement of Fracture Toughness." American Society for Testing and Materials ASTM International West Conshohocken (2015).

Brocks W and Scheider I (2001). "Numerical Aspects of the Path-Dependence of the *J*-Integral in Incremental Plasticity." *GKSS Forschungszentrum, Geesthacht* 1: 1–33.

Gianetto JA, Tyson WR, Park DY, Shen G, Lucon E, Weeks TS, Quintana MA, Rajan VN, and Wang YY (2011). "Small Scale Tensile, Charpy V-Notch, and Fracture Toughness Tests for Project Weld Design." DOT Agreement DTPH56-07-T-000005, Topical Report 277-T-05. September 2011.

Hirmand MR, Tyson WR; Xu, Su, Weeks TS (2021). "*J*-Integral Approach to Estimation of Tensile Strain Capacity in Strain-Based Design." *CanmetMATERIALS Open Technical Report*, Report No. CMAT-2021-WF 63142104.

Liu M, Wang YY, Horsley D, and Nanney S (2012). "Multi-Tier Tensile Strain Models for Strain-Based Design: Part 3—Model Evaluation Against Experimental Data." *In International Pipeline Conference*, 45158:427–38. American Society of Mechanical Engineers.

Liu M, Wang YY, and Long X (2010). "Enhanced Apparent Toughness Approach to Tensile Strain Design." (2010) 187–194. doi:10.1115/IPC2010-31386.

Liu M, Wang YY, Song Y, Horsley D, and Nanney S (2012). "Multi-Tier Tensile Strain Models for Strain-Based Design: Part 2—Development and Formulation of Tensile Strain Capacity Models." *In International Pipeline Conference*, 45158:415–25. American Society of Mechanical Engineers.

Nourpanah N, and Taheri F (2010). "Development of a Reference Strain Approach for Assessment of Fracture Response of Reeled Pipelines." *Engineering Fracture Mechanics* 77 (12): 2337–53.

Park DY, Tyson WR, Gianetto JA, Shen G, Eagleson RS, Lucon E, and Weeks TS (2011). "Small Scale Low Constraint Fracture Toughness Test Results." Final Report 277-T-06 to PHMSA, September 2011.

Park DY and Gianetto JA (2019), Review of Tensile Strain Capacity Prediction Models for Strain-Based Design of Pipelines. *In ASME Pressure Vessels and Piping Conference*, PVP2019-93220, vol. 58981, Paper No. V06BT06A042.

Shen G, Bouchard R, Gianetto JA, and Tyson WR (2008). "Fracture Toughness Evaluation of High Strength Steel Pipe." *In ASME Pressure Vessels and Piping Conference*, 48296:1275–82.

Shen G, Bouchard R, Gianetto JA, and Tyson WR (2008). "Development of Procedure for Low-Constraint Toughness Testing Using a Single-Specimen Technique." in: *ASME Press. Vessel. Pip. Conf.*, 2008: pp. 1275–1282.

Wang YY, Zhou H, Tyson WR, Gianetto JA, Quintana MA, and Weeks TS (2011). "Curved Wide Plate Test Results and Transferability of Test Specimens For Project Weld Design, Testing, and Assessment Procedures for High Strength Pipelines." DOT Agreement DTPH56-07-T-000005, Topical Report 277-T-11. January 21, 2012.

Wang YY, Liu M, Song X, Stephens M, Petersen R, and Gordon R (2011). "Second Generation Models for Strain-Based Design." PRCI Project ABD-1, US DOT Agreement DTPH56-06-T000014, Final Report, August 30, 2011.

Weeks TS, McColskey JD, and Richards M (2011). "Weld Design, Testing, and Assessment Procedures for High-Strength Pipelines Curved Wide Plate Tests For Project Weld Design, Testing, and Assessment Procedures for High Strength Pipelines." DOT Agreement DTPH56-07-T-000005, Topical Report 277-T-09. September, 2011.

Xu S, Bouchard R, and Tyson WR (2004). "Constitutive Equation for Structural Steels." *Metallurgical and Materials Transactions* A 35 (4): 1410–14.

Xu S, and Tyson WR (2015). "Effects of Strain Rate on Strength, and of Orientation on Toughness, of Modern High-Strength Pipe Steels." *Journal of Pipeline Engineering* 14 (3): 211-224.

Zhang F, Honggang Z, Wang YY, Liu M, and Song Y (2012). "Determination of J Resistance Curves From CWP Specimens." *In International Pipeline Conference*, 45158:383–90. American Society of Mechanical Engineers.

Technology for Future and Ageing Pipelines 2021
J-integral Approach to Estimation of Tensile Strain Capacity in Strain-Based Design
M.R. Hirmand, W.R. Tyson, S. Xu and T.S. Weeks